LBGW:Nd^{3+} Phosphors for Optical Detection of Temperature in Dual Biological Windows with Improved Sensitivity

Abir Douzi[a,b], Sami Slimi[a,c], Eduard Madirov[d], Josep Maria Serres[a,c], Rosa Maria Solé[a], Ezzedine Ben Salem[b], Andrey Turshatov[d], Bryce S. Richards[d] and Xavier Mateos[a,e,*]

[a]*Universitat Rovira i Virgili (URV), Física i Cristal·lografia de Materials (FiCMA), Marcel·li Domingo 1,43007, Tarragona, Spain.*

[b]*I.P.E.I. of Monastir, Research Laboratory: Physico-chemistry of Innovative Materials LR24ES16, University of Monastir 5019, Tunisia.*

[c]*Eurecat, Centre Tecnològic de Catalunya, C. Marcel·lí Domingo 2, 43007, Tarragona, Spain.*

[d]*Institute of Microstructure Technology, Karlsruhe Institute of Technology, Hermann-von-Helmholtz-Platz 1, 76344 Eggenstein-Leopoldshafen, Germany.*

[e]*Serra Húnter Fellow.*

**Corresponding author, e-mail: xavier.mateos@urv.cat*

Abstract

In this study, neodymium-doped $Li_3Ba_2Gd_3(WO_4)_8$ (LBGW:*x* Nd^{3+}) phosphors were synthesized via a conventional solid-state method and investigated for optical sensing of temperature. Upon near-infrared (NIR) excitation at 808 nm, three prominent infrared emission bands were observed, corresponding to the $^4F_{3/2} \rightarrow {}^4I_{9/2}$, $^4F_{5/2} \rightarrow {}^4I_{11/2}$, and $^4F_{3/2} \rightarrow {}^4I_{11/2}$ transitions of Nd^{3+} ions, falling within the first and second biological windows (I-BW and II-BW), and thus enabling biologically compatible optical thermometry. Temperature-dependent fluorescence intensity ratio (FIR) analysis was carried out in the 303–473 K range using three emission band pairs derived from five emission lines: P1 and P2 from $^4F_{3/2} \rightarrow {}^4I_{9/2}$, P3 from $^4F_{5/2} \rightarrow {}^4I_{11/2}$ transition, and P4 and P5 from $^4F_{3/2} \rightarrow {}^4I_{11/2}$. The three evaluated FIR schemes (P2/P1, P3/P1, and P5/P4) demonstrated distinct thermal responses, with FIR(P3/P1) exhibiting the highest relative sensitivity of 1.53 % K^{-1} and a thermal resolution of 8.86×10^{-5} K at 303 K. The phosphors also demonstrated excellent repeatability, photostability, and thermal reversibility over multiple heating–cooling cycles, confirming their robustness for non-contact, high-resolution temperature sensing. These results position LBGW:Nd^{3+} phosphors as a promising candidate for advanced optical thermometry, especially within I-BW and II-BW, where NIR emission enables compatibility with biomedical applications.

Keywords: Quaternary tungstate, Neodymium, Fluorescence intensity ratio, Optical thermometry, Biological application.

1. Introduction

Temperature is a fundamental physical parameter, and its precise and reliable measurement is essential for a wide range of industrial and scientific applications. The capability to monitor and regulate temperature with accuracy is crucial for ensuring efficiency, safety, and optimal performance in various processes [1,2]. Currently, conventional thermometers encompass various types, including liquid-filled glass thermometers that operate on the principle of thermal expansion, thermocouples that rely on the Seebeck effect, optical sensors, and other mechanisms [1]. However, in certain conditions – such as exposure to strong electromagnetic fields, operation in extreme environments, or applications involving dimensions smaller than 10 μm – conventional temperature sensors become impractical or ineffective [1,3]. To address these limitations, various research groups have focused on developing miniaturized luminescent temperature sensors. These sensors leverage different phosphors, including quantum dots, organic dyes, semiconductors and lanthanide-doped particles, to enable precise temperature measurements in challenging environments [1,3,4]. Among numerous proposed approaches, luminescent thermometers utilizing solid-state hosts doped with trivalent lanthanide ions (Ln^{3+}) have garnered significant research interest since the 1970s [3,5,6]. These luminescent probes are synthesized through different fabrication techniques, enabling their application in advanced optical sensing technologies [1,3].

Various techniques have been explored for temperature measurement using Ln^{3+}-doped phosphors [7–10]. Among these, ratiometric methodologies have received significant attention and have been extensively investigated [2,11–16]. These methods are based on the relative variation in emission intensity associated with transitions from two excited states to lower-energy levels in Ln^{3+}. The sensitivity and overall performance of these optical sensors are governed by a variety of factors, including the energy separation between emission levels, the degree of thermal coupling, the concentration and selection of dopant ions, and the chemical composition and structural properties of the host matrix.

Ln^{3+}-based luminescent thermometers have found widespread use across various scientific and technological domains [1,3,4,17–20]. Notably, their application in biological systems has been extensively explored in recent years, demonstrating significant potential for biomedical and biophysical research [17,19,21,22]. For an effective sensing system, several key requirements must be met. First, it should operate with excitation and emission wavelengths in the infrared region of the electromagnetic spectrum, specifically within the biological windows (BWs), to ensure deep tissue penetration with minimal scattering. Additionally, the system must be capable of producing strong luminescence at low excitation power, optimizing energy efficiency and reducing potential photodamage. Another crucial factor is biocompatibility, meaning the materials used should exhibit low toxicity to ensure safe application within living organisms. Lastly, the sensor must demonstrate high sensitivity to detect even slight temperature variations with precision. This can be accomplished by employing sensing schemes where both the excitation source and emitted light are selected within specific wavelength ranges, known as BWs: the first (I-BW, 700–950 nm), second (II-BW, 1000–1350 nm), and third (III-BW, 1500–1750 nm). Furthermore, luminescent probes with high absorption and emission efficiency are essential to minimize the adverse effects associated with prolonged tissue exposure to intense excitation power. A well-balanced integration of these requirements would result in temperature sensors capable of detecting minute variations in temperature, even at great depths in biological tissue or at the cellular level [1,17]. These materials intrinsically

possess high absorption and emission cross sections in the I-BW and II-BW, a feature attributed to the structured intra-4f energy scale of Nd^{3+} ions. Additionally, the small energy separations between the levels and Stark sublevels of Nd^{3+} (< 2000 cm^{-1}) enable strong thermal coupling between various level pairs. This characteristic can be leveraged for temperature measurement using ratiometric techniques, offering high sensitivity within the physiological temperature range (293–333 K), which is critical for monitoring most biological and physiological processes [2,13,15]. In this approach, infrared light sources tuned around 800 nm were employed to excite Nd^{3+} ions, while temperature was determined by analyzing the luminescence corresponding to transitions from the Stark sublevels of the $^4F_{3/2}$ excited state to the $^4I_{9/2}$ and $^4I_{11/2}$ levels. Notably, relative sensitivities as high as 0.1 $\%K^{-1}$ have been reported using this technique [13,23–26]. However, Nd^{3+}-based temperature sensing is not limited to the I-BW. Recent studies have demonstrated that by exploiting emissions around 1060 nm, it is possible to operate within II-BW, achieving deeper tissue penetration and reduced light scattering [27][28].

In 2014, Tian *et al.* [2] demonstrated FIR-based temperature sensing using $NaYF_4:Nd^{3+}$ microcrystals. Their method exploited emission bands associated with transitions from various thermally coupled level pairs to the $^4I_{9/2}$ state, specifically $^4F_{5/2}$ / $^4F_{3/2}$, $^4F_{7/2}$/$^4F_{5/2}$, and $^4F_{7/2}$/$^4F_{3/2}$, enhancing sensitivity and measurement accuracy. In addition, Kalinichev *et al.* [29] and Balabhadra *et al.* [15] have effectively implemented comparable strategies. In addition, other studies have explored infrared excitation beyond biological windows, in particular at 980 nm [27,28,30–32]. Therefore, the development of alternative high-sensitivity optical temperature sensing techniques based on Nd^{3+}-doped solid-state hosts, where both excitation and emission wavelengths reside within a biological window, represents a significant scientific and technological challenge. Among luminescent hosts, recent studies have demonstrated that quaternary tungstate compounds, particularly $Li_3Ba_2Gd_3(WO_4)_8$ (LBGW), exhibit highly efficient luminescence when doped with Ln^{3+} ions such as Pr^{3+} [33], Tb^{3+} [34], Sm^{3+} [35], Dy^{3+} [36], and Eu^{3+} [37]. These phosphors have garnered significant interest for LED applications and long-lasting luminescent materials. However, the potential of Ln^{3+}-doped LBGW for optical temperature sensing remains largely unexplored, necessitating further investigation.

In this study, we successfully synthesized Nd^{3+}-doped LBGW phosphors via the solid-state method for optical temperature sensing. Their structural, morphological, and photoluminescence properties were systematically characterized. Various FIR sensing schemes were evaluated, and their thermal sensitivities were estimated. Leveraging these properties, we propose a novel ratiometric thermometric approach based on Nd^{3+}-doped LBGW phosphors, using infrared excitation and emissions entirely within the I-BW and II-BW.

2. Materials and methods

2.1. Synthesis and Materials

LBGW:$x$$Nd^{3+}$ samples were synthesized using the conventional solid-state reaction method. The raw materials employed were of high purity: Li_2CO_3 (>99%, Alfa Aesar), $BaCO_3$ (99.9%, chemPUR), Gd_2O_3 (99.99%, Treibacher AG), Nd_2O_3 (99.99%, Treibacher AG), and WO_3 (99.9%, Honeywell Fluka). These reagents were accurately weighed according to their stoichiometric ratios and carefully mixed in an agate mortar to ensure homogeneity. The resulting powder mixture underwent a preliminary calcination at 650°C for 7 hours, favouring the decomposition of the carbonate, the elimination of volatile substances and the initiation of the reaction in the solid state. After cooling to room-temperature (RT) and fine grinding of the

calcined powder, the material was pressed into pellets to improve densification and reaction kinetics. These pellets were then subjected to a second calcination at 800°C for 14 hours in an oxygen-rich atmosphere to ensure complete phase formation and remove residual CO_2 from carbonate decomposition. To avoid structural defects and undesirable phase transitions, the samples were gradually cooled to RT. Finally, the powders were stored in a desiccator to protect them from moisture before characterization.

2.2. Measurements

The crystal structure of the synthesized LBGW:xNd^{3+} powders was examined using X-ray powder diffraction (XRD). The diffraction data were collected with a Bruker-AXS D8-Advance diffractometer, equipped with a vertical θ–θ goniometer and operating with Cu Kα radiation (λ = 1.5406 Å). To detect the diffracted X-rays, a LynxEye-XE-T position-sensitive detector with an opening angle of 2.94° was utilized, ensuring high precision and resolution in the measurements. For Rietveld refinement, the diffraction data were recorded with a step size of 0.02° and a step time of 2 seconds, covering a 2θ range from 10° to 80°. The sample was supported on Si(510), chosen for its low background interference. The refinement process was carried out using the Match crystal impact (Version 4) software to ensure accurate structural analysis. The elemental composition of the samples was analyzed using energy-dispersive X-ray spectroscopy (EDX). The measurements were carried out with a FEI Quanta 600 environmental scanning electron microscope (ESEM) equipped with an Oxford Inca 3.0 microanalyzer. Raman spectra were acquired using a Renishaw InVia confocal Raman microscope, which was equipped with an edge filter, a 50× objective, and an Ar^+ ion laser as excitation source (λ_{ex}= 514 nm). A Varian Cary 5000 UV-Vis-NIR spectrophotometer, equipped with an integrating sphere, was used to measure the reflectance spectra at RT. The measurements were performed on 12 mm diameter pellet samples over a spectral range of 200–850 nm, with a data interval of 0.5 nm and an integration time of 1 second. To carry out the luminescence measurements, we used a custom-built system comprising an optical spectrum analyzer (OSA AQ6373E- Yokogawa Electric Corporation) connected to a detector and equipped with an AlGaAs diode laser (Ostech) emitting at 808 nm in continuous-wave (CW) mode, with a maximum output power of 15 W. The excitation power density at the sample surface was approximately 101.9 W/cm^2. Luminescence lifetime measurements were performed using a cooled photomultiplier tube (R928P, Hamamatsu) and a dual monochromator (DTMS300, Bentham) to select the emission wavelength. In addition, a temperature-controlled device in which high-resolution thermocouple sensor was used for temperature monitoring, was specially configured to record sample emission spectra as a function of temperature between 303 and 473 K.

3. Results and discussion

3.1. Structural properties

The series of quaternary tungstate samples, LBGW:x Nd^{3+} (x = 0, 1, 2, 3, 4, and 5 at.%), were analyzed using XRD to confirm their phase purity. Fig.1(a) presents the XRD patterns of all synthesized samples, confirming their crystalline nature and their association with the quaternary tungstate LBGW-type structure. The diffraction patterns align with the JCPDS (Joint Committee on Powder Diffraction Standards) #7211787, corresponding to the Nd:$Li_3Ba_2Y_3(WO_4)_8$ crystal, as illustrated in Fig.1(b). The XRD analysis revealed no evidence of secondary phases in the samples with the investigated Nd concentrations, confirming their

homogeneous single-phase composition. LBGW:*x* at.% Nd^{3+} phosphors crystallise in the monoclinic class with the *C2/c* space group and the *2/m* point group. The sharpness and intensity of the observed diffraction peaks indicate the high crystallinity of the samples, which is a key factor in improving the optical efficiency of the phosphors.

According to Shannon's reference, the ionic radii of Nd^{3+}, Gd^{3+}, Li^{+}, and Ba^{2+} in eightfold coordination are as follows: Nd^{3+} (1.109 Å), Li^{+} (0.92 Å), Ba^{2+} (1.42 Å), and Gd^{3+} (1.053 Å) [38]. Among them, Gd^{3+} has the closest ionic radius to Nd^{3+} while preserving the same charge state, making it a favorable candidate for substitution within the crystal lattice. In LBGW, Nd^{3+} ions are expected to replace the trivalent host cations, Gd^{3+}, primarily at the 8f crystallographic sites. This substitution is anticipated to increase the lattice constants, resulting in structural modifications within the crystal lattice. The substitution of Gd^{3+} ions in the lattice by Nd^{3+} is confirmed by the percentage difference in ionic radii (Δr) between the Nd^{3+} activator and the Gd^{3+} host ion, calculated using Equation (1) [38]:

$$\Delta r = \left|\frac{R_h - R_d}{R_h}\right| \times 100\% \ , \qquad (1)$$

where R_d represents that of the activator ion (Nd^{3+}), and R_h denotes the ionic radius of the host ion (Gd^{3+}). The calculated Δr is approximately 5.3%. For effective integration, the difference in ionic diameters between the dopant and host ions must remain below 30% [39]. This value of Δr is sufficiently small to facilitate the substitution of Gd^{3+} by Nd^{3+} in the crystal lattice, suggesting that Nd^{3+} ions can be successfully incorporated into the LBGW host without inducing significant structural distortion, which is consistent with the phase purity observed in XRD patterns.

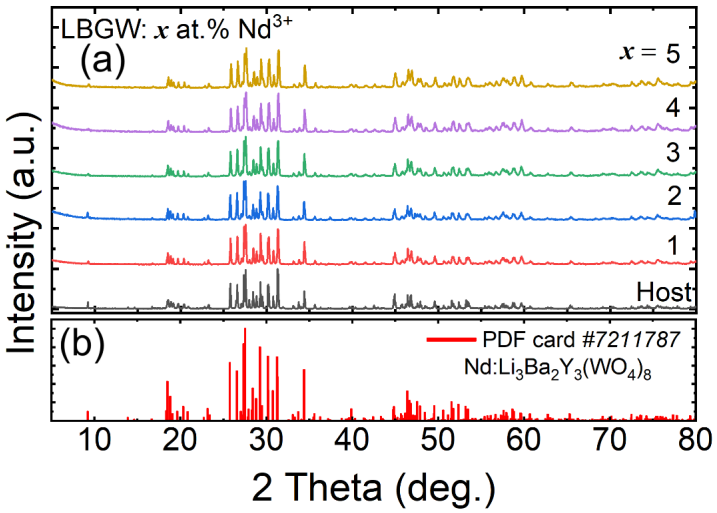


Figure 1. (a) XRD patterns of LBGW:*x* Nd^{3+} phosphors with x= 0, 1, 2, 3, 4, and 5 at.%, (b) Standard powder diffraction pattern of $Nd:Li_3Ba_2Y_3(WO_4)_8$.

To gain a deeper insight into the structure of LBGW:*x* Nd^{3+} phosphors and the incorporation behavior of Nd^{3+} ions within the LBGW host matrix, a Rietveld refinement was performed for the LBGW:3 at% Nd^{3+} sample. The fitted diffraction pattern is presented in Fig. 2(a), while the corresponding refinement parameters are summarized in Table 1. The $Nd:Li_3Ba_2Y_3(WO_4)_8$ structure served as the reference model for the Rietveld refinement process [40]. The calculated profiles exhibit a strong correlation with the experimental data. The refined lattice parameters for the LBGW: 3 at.% Nd^{3+} sample are as follows: ***a*** = 5.217(5) Å, ***b*** = 12.747(4) Å, and ***c*** =

19.203(7) Å, with a calculated unit cell volume of $V = 1276.591(1)$ Å^3. The monoclinic structure is defined by an angle $\beta = 91.84(8)$ Å, while the theoretical crystal density is $\rho_{calc} = 7.155$ g/cm^3. The unit cell comprises two formula units (Z=2). Refinement resulted in a reduced chi-square value (Chi^2) of 1.44 and an R_{wp} factor of 8.00%, indicating a well-convergent fit with a high degree of reliability.

The atomic coordinates, crystallographic sites, isotropic displacement parameters and occupancy factors determined for sample LBGW:3 at.% Nd^{3+} are presented in Table 2. Additionally, based on the results of Rietveld refinement, a structural fragment of LBGW:Nd^{3+} was visualised along the b-c crystallographic plane, as shown in Fig.2(b).

Li^+ ions occupy two distinct crystallographic sites. The first, Li1, is statistically distributed with Gd^{3+} and Nd^{3+} ions in the structure. The second site, labelled Li2, corresponds to a special crystallographic position with the 4th Wyckoff symbol, where the atoms are coordinated by six oxygen atoms. While Ba^{2+} ions are surrounded by ten oxygen atoms, forming distorted $[Ba]O_{10}$ polyhedra. Each [Gd|Li1|Nd] site is surrounded by eight oxygen atoms, forming a distorted polyhedral structure. The polyhedra $[Li2]O_6$, $[Ba]O_{10}$, and $[Gd|Li1|Nd]O_8$ are interconnected by shared oxygen atoms, forming a cohesive structural framework. The $[Gd|Li1|Nd]O_8$ polyhedra arrange themselves into a two-dimensional layered structure parallel to the (b–c) plane. At the same time, $[Ba]O_{10}$ polyhedra connect adjacent layers of $[Gd|Li1|Nd]O_8$-$[Gd|Li1|Nd]O_8$, creating a three-dimensional network that ultimately gives rise to a single-layer polyhedral structure.

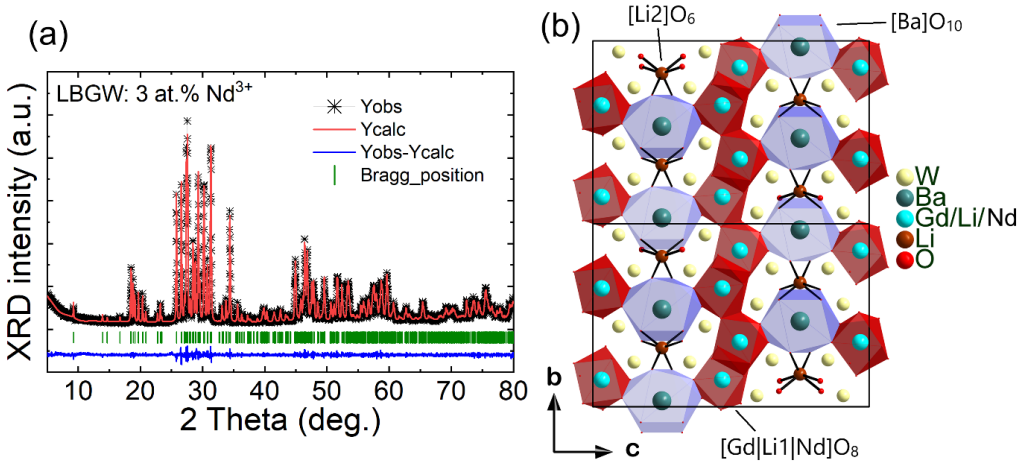


Figure 2. (a) Rietveld refinement plots and (b) fragment structure in projection on the b-c crystallographic plane for LBGW:3 at.% Nd^{3+}.

Table 1. Crystallographic data and Rietveld refinement details for LBGW:3 at.% Nd^{3+} sample

Data	LBGW**:3 at.% Nd^{3+}**
Chemical formula	$Li_3Ba_2Gd_{2.91}Nd_{0.09}(WO_4)_8$
Crystal System	monoclinic
Space group (IT number, ***Z***)	*C2/c* (15, 2)
Laue Class	*2/m*
Calculated density (g/cm^3)	7.155
Lattice constant ***a***,***b***,***c***(Å)	5.217(5), 12.747(4), 19.203 (7)
α,***β***,***γ***(deg.)	90, 91.84 (8), 90
Volume(Å^3)	1276.591 (1)
2θ range (deg.)	10-80
2θ step	0.02
Radiations	Cu-Kα1 (λ= 1.5418 Å)
Refinement software	Match crystal impact (Version 4)
Reliability factors	R_p = 6.01 %; R_{wp} = 8.00 %; R_{exp} = 6.67; Chi^2 = 1.44; Bragg R-factor= 1.83

Table 2. Atomic coordinates, sites, occupancy factors (O.F) and isotropic displacement parameters B_{iso} (Å^2) LBGW:3 at.% Nd^{3+} sample.

Atoms	**sites**	**x/a**	**y/b**	**z/c**	**O.F**	**B_{iso}(Å^2)**
W1	8f	0.4873(3)	0.4412(3)	0.4055(0)	1.000	1.256(1)
W2	8f	0.5001(7)	0.7523(6)	0.3513(3)	1.000	0.833(1)
Ba	4e	1.0000(0)	0.5335(6)	0.2500(0)	1.000	1.584(6)
Gd|Li1|Nd	8f	1.0045(0)	0.6546(8)	0.4695(8)	0.728|0.250|0.022	0.779(2)
Li2	4e	0.5000(0)	0.3253(0)	0.2500(0)	1.000	1.795(4)
O1	8f	0.6423(0)	0.4148(0)	0.3263(0)	1.000	2.921(1)
O2	8f	0.2565(5)	0.5433(9)	0.4039(0)	1.000	2.843(7)
O3	8f	0.7726(9)	0.4613(1)	0.4459(1)	1.000	2.468(4)
O4	8f	0.3025(3)	0.3361(1)	0.4520(9)	1.000	2.134(8)
O5	8f	0.2245(6)	0.7156(9)	0.2898(8)	1.000	2.665(7)
O6	8f	0.7395(9)	0.6502(1)	0.3600(0)	1.000	2.987(1)
O7	8f	0.6685(0)	0.8441(7)	0.3299(8)	1.000	2.331(5)
O8	8f	0.2955(5)	0.7405(0)	0.4201(5)	1.000	2.438(4)

Fig. 3(a) displays an ESEM micrograph of LBGW doped with 3 at.% Nd^{3+} and annealed at 900°C, revealing particles that predominantly exhibit spherical and blocky morphologies. These particles have irregular shapes and a broad size distribution ranging from 0.5 to 3 μm. The micrometric size of the powdered samples does not pose a limitation for their potential use in biological applications. In fact, dispersed microparticles within the 0.5–10 μm range are suitable for various biomedical applications, including drug delivery in cancer immunotherapy [41] and treatments for infectious diseases [42]. Unlike nanoparticles, which are internalized by cells through endocytosis, microparticles are primarily taken up via phagocytosis [41].

These particles exhibit a tendency to grow and agglomerate, forming large aggregates exceeding 5 μm in size, likely driven by Van der Waals interactions between the particles [43]. The sample composition was characterized using line-scan EDX and elemental mapping. Representative EDX spectra for LBGW:3 at.% Nd^{3+}sample are depicted in Fig. 3(b), while the corresponding elemental mapping is shown in Fig. 3(c). For the Nd^{3+}-doped sample, the presence of Nd as an additional dopant is distinctly evident. Elemental mapping of Nd and Gd

confirms a uniform distribution of the dopant within the host matrix, aligning with the findings from the XRD analysis.

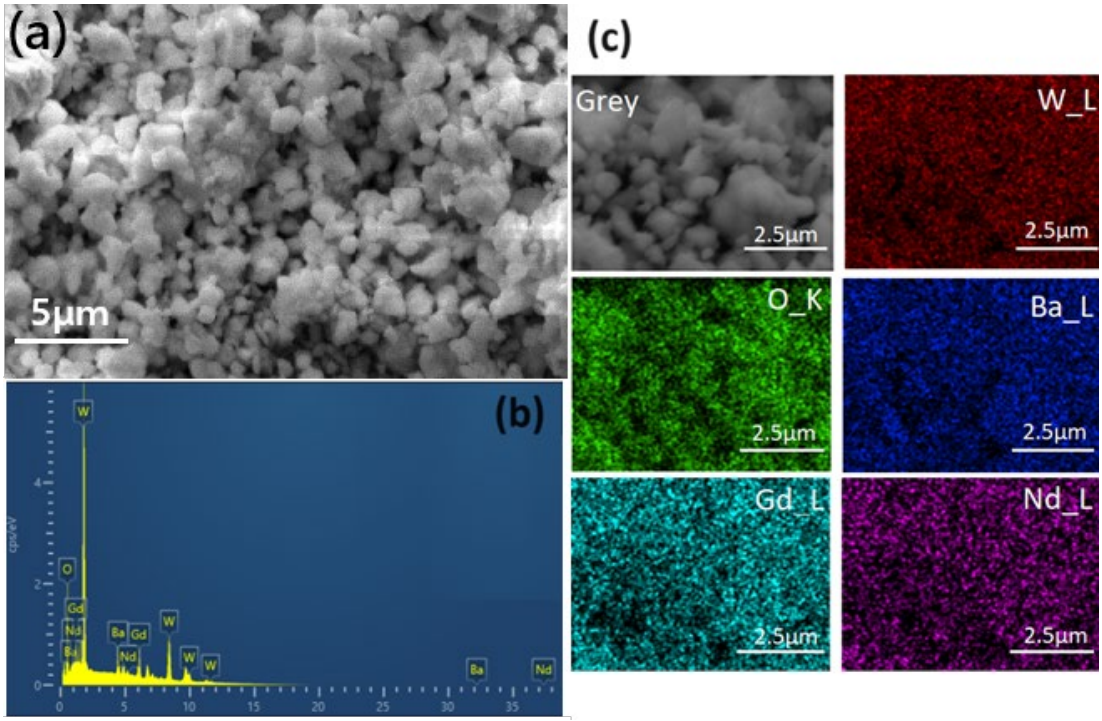


Figure 3. (a) ESEM image (b) Energy-dispersive X-ray (EDX) spectra (c) elemental mapping for the LBGW:3 at.% Nd^{3+}.

The Raman spectra of LBGW:*x* Nd^{3+} (with *x*=1, 2, 3, 4, and 5 at.%) were recorded under ambient conditions, corresponding to RT and normal atmospheric pressure, using a 514 nm excitation source. The spectra, shown in Fig. 4, cover the range of 100–1200 cm^{-1} and reveal several characteristic vibrational modes. Consistent with observations reported in prior research [36,44], the modes centered at 913 cm^{-1} and 888 cm^{-1} are assigned to the symmetric stretching vibrations of the $(WO_4)^{2-}$ tetrahedra, while the modes at 840 cm^{-1} , 794 cm^{-1} , and 748 cm^{-1} correspond to asymmetric stretching vibrations. The band observed at 396 cm^{-1} is attributed to the asymmetric bending of $(WO_4)^{2-}$, while the band at 325 cm^{-1} is associated with its symmetric bending. Additionally, the bands at 123 cm^{-1} and 213 cm^{-1} are linked to lattice vibrations, as previously reported. At 640 cm^{-1}, the band is attributed to an oxygen stretching vibration associated with a long bridge, coupled with a bending vibration (δ(O-W-O)).

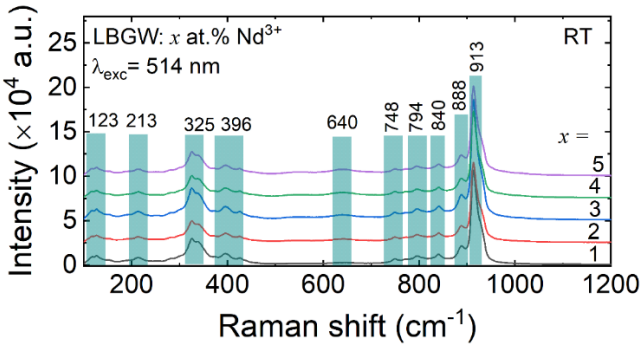


Figure 4. Raman spectra of the LBGW:*x* at.% Nd^{3+} samples for *x*= 1, 2, 3, 4, and 5.

3.2. Optical properties

Fig. 5 displays the UV-visible diffuse reflectance spectra recorded for LBGW samples with different concentrations of Nd^{3+} (denoted as x at.% Nd^{3+} and ranging from x=1 to 5) at RT. The spectra cover a wavelength range from 200 to 840 nm. Within these spectra, noticeable UV absorption is observed at approximately 256 nm, attributed to the charge transfer band (CTB) arising from $O^{2-}\rightarrow W^{6+}$ and $O^{2-}\rightarrow Nd^{3+}$ interactions. Several optical bands were detected in the diffuse reflectance spectra of LBGW:Nd^{3+} phosphors above 300 nm. These distinct absorption bands correspond to transitions of Nd^{3+} ions from the ground state $^4I_{9/2}$ to various excited states, namely $^2P_{1/2}+{}^2D_{3/2}$, $^4G_{11/2}$, $^2K_{13/2}+{}^4G_{9/2}$, $^4G_{7/2}$, $^4G_{5/2}$, $^2H_{11/2}$, $^4F_{9/2}$, $^4F_{7/2}+{}^4S_{3/2}$, and $^4F_{5/2}+{}^2H_{9/2}$, located approximately at 337, 374, 516, 529, 586, 630, 685, 751, and 804 nm, respectively [45,46]. Hence, near-ultraviolet LEDs can serve as the excitation source for LBGW:Nd^{3+} phosphors.

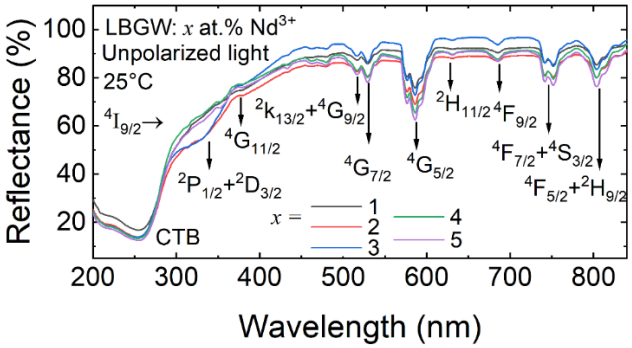


Figure 5. UV-visible diffuse reflectance spectra of LBGW:x at.% Nd^{3+} phosphors with x= 1, 2, 3, 4 and 5.

The optical energy bandgap of prepared phosphors LBGW:$x$$Nd^{3+}$ (where x=1, 2, 3, 4, and 5 at.%) was estimated from reflectance spectra using the following equation [47]:

$$[F(R_\infty)h\upsilon]^n = A\left(h\upsilon - E_g\right), \quad (2)$$

where, E_g denotes the optical bandgap value, $h\upsilon$ represents the energy of a photon, A is a constant, and $F(R_\infty)$ refers to the Kubelka-Munk function, defined as:

$$F(R_\infty) = \frac{(1-R)^2}{2R} = \frac{K}{S}. \quad (3)$$

In this expression, K, S, and R stand for the absorption, scattering, and reflection coefficients, respectively. The bandgap of the prepared phosphors was determined through the analysis of diffuse reflection spectra utilizing Kubelka-Munk theory [48]. The relationship between the E_g and the linear absorption coefficient K of a material is established by the well-known Tauc relation [49]. By examining the graph of $[F(R_\infty)h\upsilon]^2$ against $h\upsilon$, the E_g value was derived by extending the linearly fitted sections to $[F(R_\infty)h\upsilon]^2 = 0$, as illustrated in Fig. 6.

The calculated E_g values for LBGW:$x$$Nd^{3+}$ phosphors were found to be 2.82 eV, 2.84 eV, 2.86 eV, 2.87 eV, and 2.89 eV for x = 1, 2, 3, 4, and 5 at.%, respectively. Among all samples, LBGW:5 at.% Nd^{3+} phosphors exhibit the highest bandgap energy. As shown in Fig. 6, the bandgap energy gradually increases with increasing Nd^{3+} concentration, ranging from 2.82 to 2.89 eV as the doping level rises from 1 to 5 at.%, indicating a systematic shift in the optical properties of the host matrix with dopant incorporation.

Furthermore, in our previous study carried out in our laboratory, we determined that the experimental optical bandgap of the LBGW host was 2.79 eV [36], showing that the incorporation of Nd^{3+} ions into this host lattice leads to a slight increase in the bandgap value. This can be attributed to the structural disruption that occurs in the host lattice due to the incorporation of dopant Nd^{3+} ions [37].

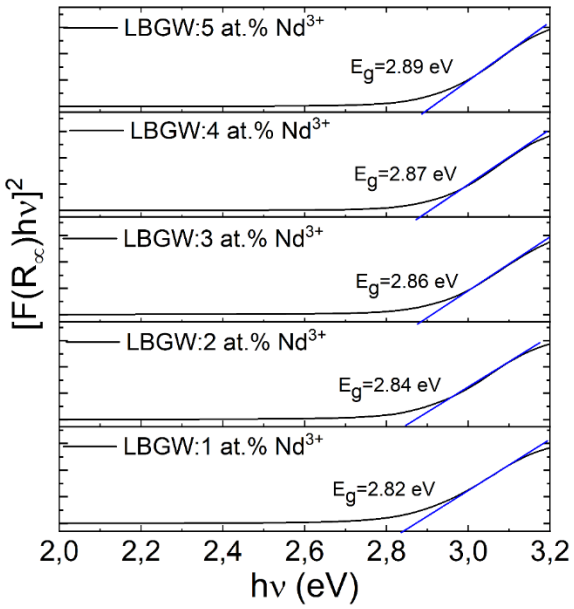


Figure 6. Calculated E_g of LBGW:*x* Nd^{3+} phosphors (*x*=1, 2, 3, 4, and 5 at.%) from the diffuse reflectance spectra.

The photoluminescence (PL) properties of LBGW:*x* at.% Nd^{3+} samples (*x*=1, 2, 3, 4, and 5) were analyzed at RT using an 808 nm CW laser as the excitation source. The NIR emission spectra, presented in Fig. 7(a), reveal three prominent emission features characteristic of Nd^{3+}-doped materials [50,51]. The first is a broad emission band with Stark sublevels, spanning 872–912 nm with a maximum at 872 nm, corresponding to the $^4F_{3/2}\rightarrow{}^4I_{9/2}$ transition. The second is a distinct band centered at 1060 nm, covering the range from 976 to 1060 nm, attributed to the $^4F_{3/2}\rightarrow{}^4I_{11/2}$ transition. The third is a weak emission band observed between 948 and 976 nm, peaking at 950 nm, associated with the $^4F_{5/2}\rightarrow{}^4I_{11/2}$ transition. These findings confirm the characteristic emission behavior of Nd^{3+} in the synthesized samples. Apart from variations in peak intensity, all spectra show identical features, indicating that the observed excitation peaks arise exclusively from f→f transitions of Nd^{3+}. This observation aligns with the fact that the ionic radii of Gd^{3+} and Nd^{3+} are similar and that they share the same trivalent charge ($^{3+}$), allowing for more efficient substitution of Nd^{3+} into the host lattice compared to other cations in the LBGW matrix [46].

The LBGW:Nd^{3+} phosphor exhibits excitation and emission wavelengths that align with the I-BW and the II-BW. Notably, the emission at 1060 nm from the Nd^{3+} ion has been widely utilized in producing NIR lasers, with materials such as YVO_4:Nd^{3+} and YAG:Nd^{3+} serving as prominent examples of Nd-based lasers. This unique combination of properties highlights the material's significant potential as a versatile candidate for a wide range of imaging, biomedical, and laser applications [46,52–54].

To elucidate the mechanism of luminescence of the LBGW:Nd^{3+} luminophore in the NIR region under 808 nm excitation, a simplified diagram of the energy levels of Nd^{3+} ions is shown in Fig. 7(b). When excited at 808 nm, Nd^{3+} ions in the ground state ($^4I_{9/2}$) are promoted to the higher energy level ($^4F_{5/2}$). These ions rapidly relax non-radiatively to the metastable state ($^4F_{3/2}$), which is the main source of radiative emissions. From the ($^4F_{3/2}$) state, two dominant emissions are observed: one at 872 nm, corresponding to the $^4F_{3/2}\rightarrow{}^4I_{9/2}$ transition, and the other at 1060 nm, associated with the $^4F_{3/2}\rightarrow{}^4I_{11/2}$ transition. In addition, weaker emission at 950 nm is attributed to the direct $^4F_{5/2}\rightarrow{}^4I_{11/2}$ transition.

Fig. 7(c) illustrates that, under 808 nm excitation at RT, the emission intensity of Nd^{3+} ions increases progressively with rising dopant concentration, reaching a maximum at x=3 at.%. However, beyond this threshold, the emission intensity declines as the Nd^{3+} concentration continues to increase. This decline is attributed to the concentration quenching phenomenon, driven by Nd^{3+}-Nd^{3+} interactions. As the Nd^{3+} concentration increases, energy transfer between neighboring ions becomes more pronounced, facilitating non-radiative relaxation pathways. The nature of the interaction is determined by evaluating the critical distance (Rc). When Rc exceeds 5 Å, the interaction is predominantly governed by electric multipolar mechanisms. Conversely, if Rc is below 5 Å, exchange interactions become the dominant energy transfer process. Equation (4), as formulated by Blasse [55], provides a means to calculate the Rc:

$$Rc = [\frac{3V}{4\pi x_c Z}]^{1/3}\ , \tag{4}$$

where Z represents the number of cationic sites occupied by activator ions within a single unit cell, V corresponds to the unit cell volume, and x_c denotes the critical concentration. In our study, the specific parameters for LBGW:Nd^{3+} phosphors are V=1276.591 Å^3, Z=2, and x_c=0.03. The calculated Rc is 17.19 Å, which significantly exceeds the threshold value (Rc≥5 Å). This suggests that the energy transfer mechanism in LBGW:Nd^{3+} is likely governed by electric multipolar interactions.

According to Dexter's theory [56], this type of interaction between neighboring Nd^{3+} ions can be further analyzed using the provided Equation (5):

$$\frac{I}{x} = K[1+\beta(x)^{\frac{\theta}{3}}]^{-1} \tag{5}$$

In the rearrangement of Equation (5):

$$Ln\left(\frac{I}{x}\right) = K' - (\frac{\theta}{3} lnx)\ , \tag{6}$$

where I denotes the emission intensity, K' and β are constants specific to a given host lattice, while θ defines the type of interaction between the emitting ions. Additionally, x represents the activator concentration. When θ takes values of 6, 8, and 10, it signifies dipole-dipole, dipole-quadrupole, and quadrupole-quadrupole interactions, respectively.

The inset of Fig. 7(c) displays a plot of ln(I/x) versus ln(x) for the emission at 1060 nm, corresponding to the $^4F_{3/2}\rightarrow{}^4I_{11/2}$ transition in LBGW:Nd^{3+} phosphors. The linear fitting was performed over the full concentration range (x = 1–5 at.%), and the data exhibit a clear linear trend with a high correlation coefficient (R^2 = 0.99). The slope of the fitted line is (−θ/3) = −1.89, resulting in a calculated θ value of 5.67. This value, being close to 6, indicates that energy transfer among Nd^{3+} ions in LBGW primarily occurs via dipole–dipole interactions.

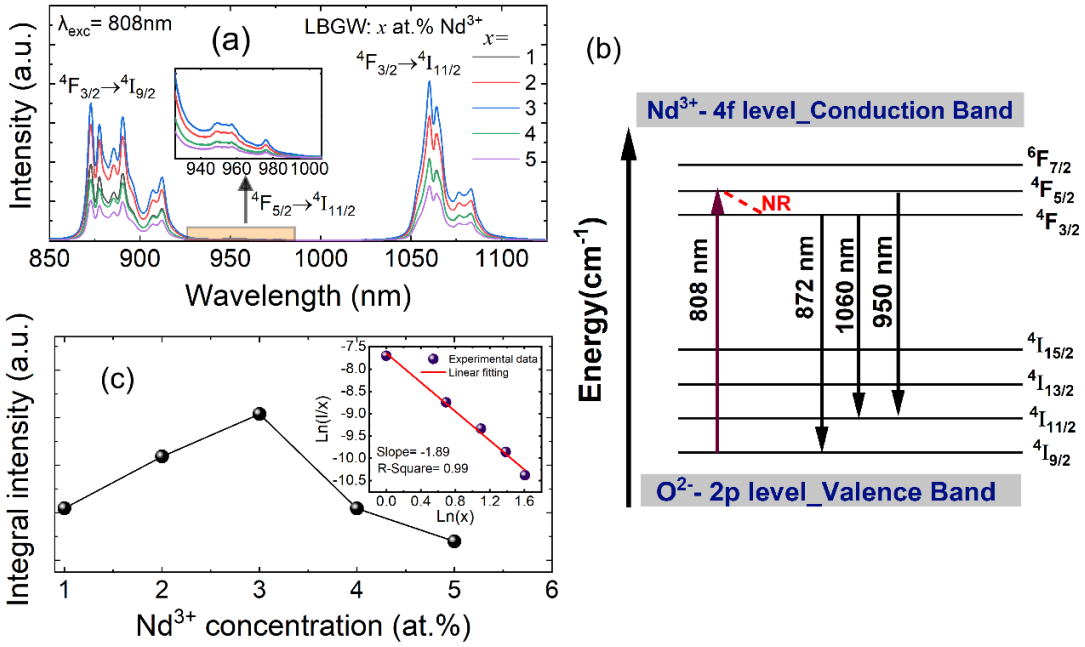


Figure 7. (a) Emission spectra of LBGW:*x* at.% Nd^{3+} phosphors with *x*= 1, 2, 3, 4, and 5 under 808 nm excitation. (b) Simplified energy level diagram of Nd^{3+} ion in LBGW matrix (NR = non-radiative transitions). (c) Variation of the integral intensity of the $^4F_{3/2} \rightarrow {}^4I_{11/2}$ emission band as a function of Nd^{3+} concentration; (inset: analysis of the type of interaction using the Dexter equation; *x*- Nd^{3+} concentration, I - luminescence intensity).

The luminescence decay curves of LBGW: *x* at.% Nd^{3+} phosphors, with doping levels *x*=1, 2, 3, 4, and 5, measured at RT, are presented in Fig. 8(a). These measurements were performed under excitation at λ_{exc}=808 nm, with emission monitored at λ_{lum}=1060 nm, corresponding to the decay from the metastable $^4F_{3/2}$ excited state. The decay profiles are accurately described by a single-exponential function, as given by the Equation (7):

$$I(t) = I_0 \exp(-\frac{t}{\tau_{lum}}) , \quad (7)$$

where I(t) is the PL intensity at time t, I_0 is the initial intensity, and τ_{lum} represents the luminescence lifetime. Fig. 8(b) demonstrates the excellent agreement of the mono-exponential fit with the decay curve measured for the sample doped with *x*=3 at.% Nd^{3+}. For the $^4F_{3/2}$ level of Nd^{3+} in LBGW samples doped with *x* at.% Nd^{3+} (*x*=1, 2, 3, 4, and 5), the corresponding luminescence lifetimes are 0.193, 0.192, 0.184, 0.176, and 0.161 ms, respectively. The observed reduction in lifetime at higher doping concentrations provides strong evidence of non-radiative energy transfer processes occurring between Nd^{3+} ions within the LBGW matrix. As the Nd^{3+} doping concentration increases from 1 to 5 at.%, the luminescence lifetime τ_{lum} gradually decreases from 0.193 to 0.161 ms. Fig. 8(c) clearly illustrates this inverse relationship between the decay time and the Nd^{3+} doping concentration.

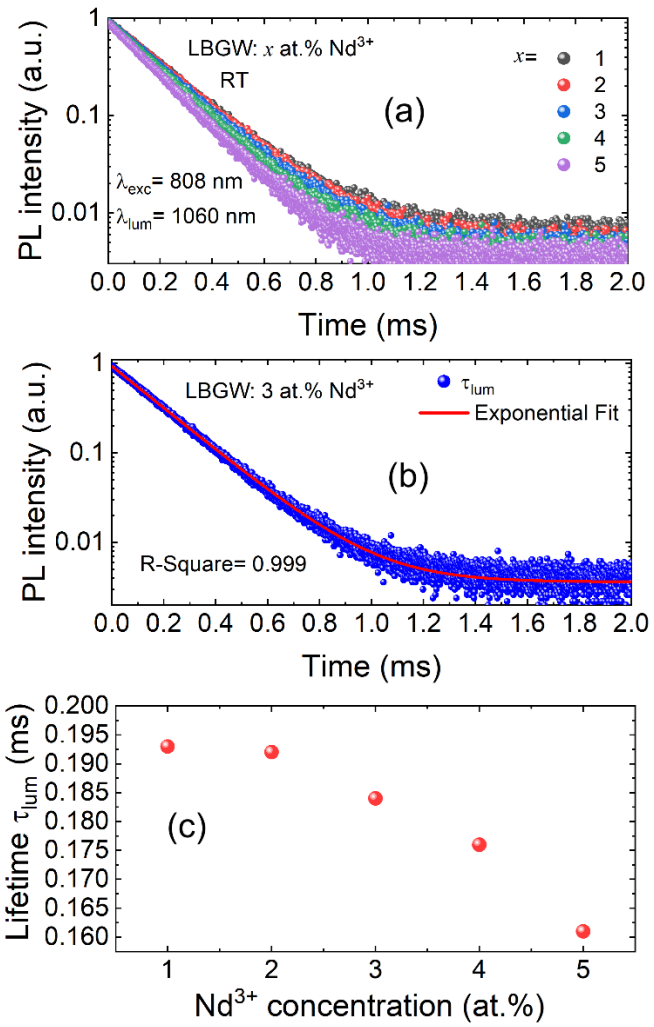


Figure 8. (a) RT luminescence decay curves for LBGW:*x* at.% Nd^{3+} phosphors under excitation at λ_{exc}=808nm and emission at λ_{lum}=1060nm; (b) mono-exponential fit of the decay curve for LBGW:3 at.% Nd^{3+} sample; (c) luminescence decay time τ_{lum} as a function of Nd^{3+} doping concentration.

3.3. Optical sensing of temperature

The effect of environmental temperature on the Nd^{3+} emission lines in LBGW was investigated to assess its potential as an optical temperature sensor. Figs. 9(a), 9(b), and 9(c) display the temperature-dependent PL spectra of LBGW:3 at.% Nd^{3+} microparticles, recorded across the wavelength ranges of 850–1000 nm and 1000–1150 nm. These spectra, collected from 303 K to 473 K in 10 K intervals, reveal clear temperature-induced variations in the intensity of five emission lines: P1 (872 nm) and P2 (885 nm) from the $^4F_{3/2} \rightarrow {}^4I_{9/2}$ transition, P3 (950 nm) from the $^4F_{5/2} \rightarrow {}^4I_{11/2}$ transition, and P4 (1060 nm) and P5 (1077 nm) from the $^4F_{3/2} \rightarrow {}^4I_{11/2}$ transition. P1, P2, and P3 lie within the first biological window (I-BW), while P4 and P5 fall into the second biological window (II-BW), supporting their potential for bio-imaging and therapeutic applications.

Under 808 nm excitation, the luminescence intensities corresponding to the $^4F_{3/2} \rightarrow {}^4I_{9/2}$ and $^4F_{3/2} \rightarrow {}^4I_{11/2}$ transitions decrease as the environmental temperature increases. In contrast, the emission intensity associated with the $^4F_{5/2} \rightarrow {}^4I_{11/2}$ transition exhibits a different trend compared to $^4F_{3/2}$ excited state, as its emission increases with rising temperature. This behavior is closely

related to the excitation and emission mechanisms of Nd^{3+} ions in the host material. The excitation of Nd^{3+} occurs through a phonon-assisted laser photon absorption process [57], in which lattice vibrations play a role in promoting electronic transitions. Due to the thermal coupling between the $^4F_{5/2}$ and $^4F_{3/2}$ levels, a temperature increase enhances the population of the higher-energy $^4F_{5/2}$ level at the expense of the $^4F_{3/2}$ state, leading to a progressive decrease in the emission intensity of $^4F_{3/2}$. Under NIR excitation, the luminescence intensity of the $^4F_{5/2} \rightarrow {}^4I_{11/2}$ transition is observed to increase with temperature, confirming the influence of thermal redistribution on the emission properties of Nd^{3+}-doped LBGW phosphors.

These spectral features enabled the calculation of three distinct FIR ratios: P2/P1, P3/P1, and P5/P4. A detailed description of the FIR methodology and sensitivity calculations is provided in the Supporting Information file. The thermal coupling between the $^4F_{5/2}$ and $^4F_{3/2}$ levels of Nd^{3+} is a well-documented phenomenon and has been widely explored for its application in temperature sensing [58–60]. Among the analyzed transitions, the FIR configuration based on the P5/P4 emission band ratio, originating from the $^4F_{3/2} \rightarrow {}^4I_{11/2}$ transition, has not previously been identified as a practical thermometric parameter. To the best of our knowledge, this study presents the first evaluation of its temperature-dependent behavior and thermometric performance in Nd^{3+}-doped LBGW phosphors. This novel approach contributes to expand the available FIR-based schemes, particularly those operating within II-BW, and offers promising sensitivity for biomedical sensing applications.

In agreement with the thermal coupling theory, the FIR between two thermally coupled excited states follows an exponential temperature dependence, as detailed in the supplementary material. Therefore, when the FIR is plotted on a semi-logarithmic scale, it should exhibit a linear trend, confirming the applicability of the Boltzmann distribution to describe population redistribution [61].

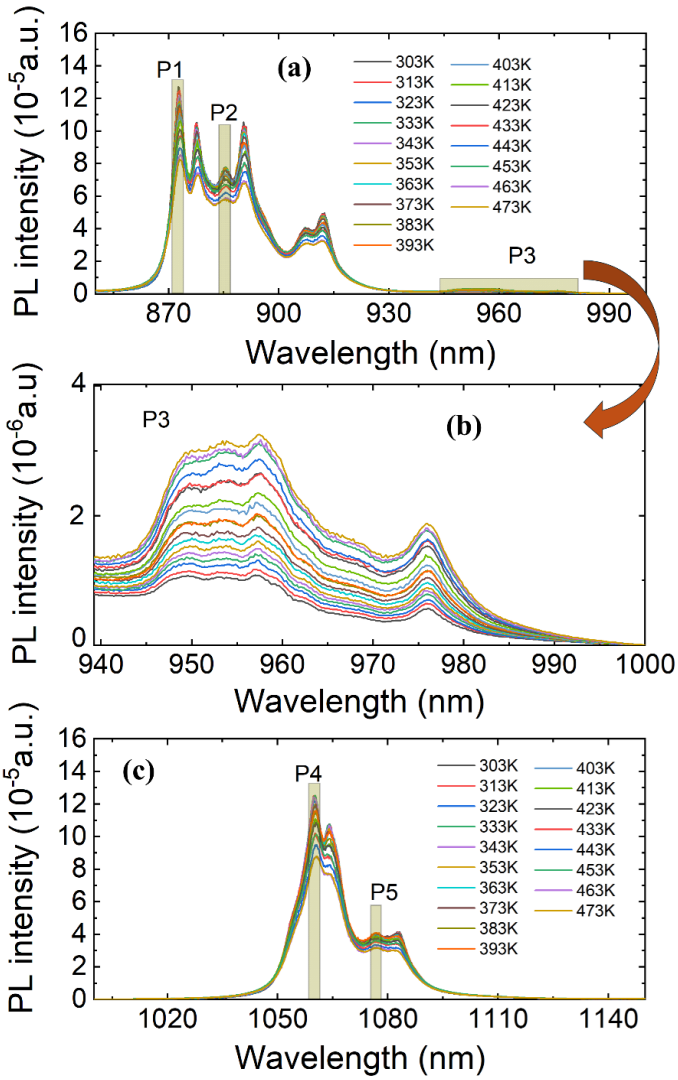


Figure 9. Temperature-dependent PL spectra of LBGW:3 at.% Nd^{3+} phosphors under 808 nm excitation: (a) Emission lines in the 850–1000 nm range, showing P1 (872 nm), P2 (885 nm), and the onset of P3. (b) Zoom in on the 939–1000 nm region highlighting P3 (950 nm) from the $^4F_{5/2} \rightarrow {}^4I_{11/2}$ transition. (c) Emission lines from 1000–1150 nm showing P4 (1060 nm) and P5 (1077 nm) from the $^4F_{3/2} \rightarrow {}^4I_{11/2}$ transition.

As shown in Fig. 10, the FIR curves exhibit an approximately linear response over a temperature range from 303 to 420 K for FIR(P2/P1) and FIR(P3/P1). However, for FIR(P5/P4), the linear behavior is maintained only up to 400 K. Within these respective ranges, increasing temperature facilitates thermally induced transitions between the low-energy and high-energy Stark sublevels, leading to a progressive increase in the upper-state population while the lower-state population decreases. This behaviour is consistent with the Maxwell-Boltzmann distribution, which governs the thermal population of energy levels in coupled systems.

However, at higher temperatures (above 420 K), additional transitions involving higher-energy levels become thermally accessible. These competing processes alter the thermal population dynamics, leading to deviations from the linear trend expected in the semi-logarithmic FIR plots. As a result, the system no longer behaves as a simple two-level thermal equilibrium model. A more comprehensive description must consider the contribution of

multiple excited states, which increasingly affect the emission behavior of Nd^{3+}-doped LBGW phosphors.

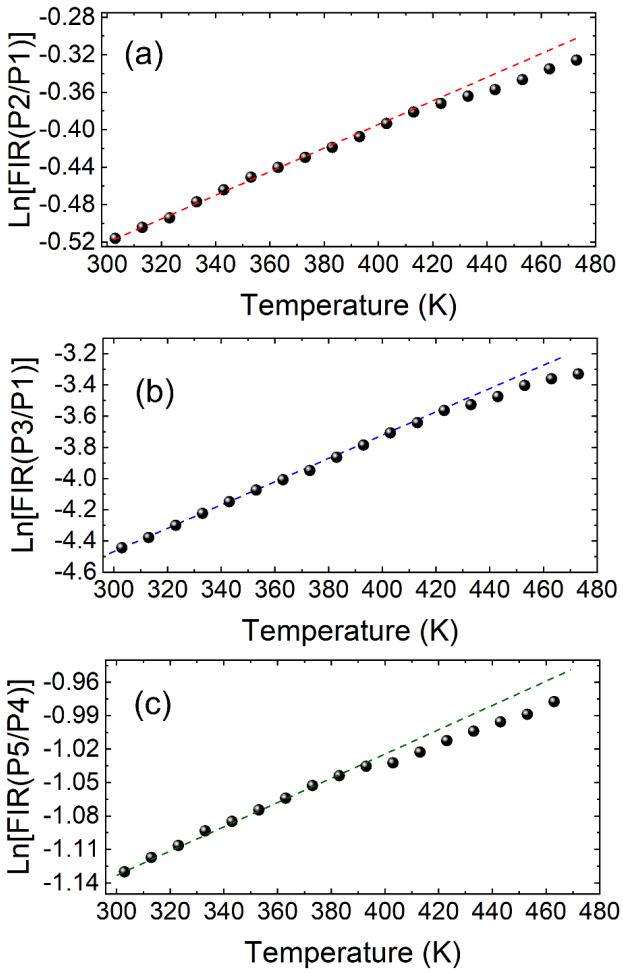


Figure 10. The behavior of the FIR signal as a function of temperature at 808 nm excitation for: (a) FIR(P2/P1), (b) FIR(P3/P1), and (c) FIR(P5/P4).

The behavior of these three FIRs is examined in Fig. 11, plotted as a function of the inverse of the environmental temperature. The red lines illustrate the exponential fits obtained using Equation (S.5). All results show a strong correlation with the expected exponential trend, which is characteristic of thermal coupling between two electronic states, where the population ratio follows the Maxwell–Boltzmann distribution. The values of y_0, A, and ΔE are displayed in the corresponding graphs. Notably, non-zero values of the offset parameter y_0 indicate the influence of spectral overlap between adjacent emission bands [62]. In the case of FIR(P3/P1) (Fig. 11(b)), the very small value of y_0 (~0.006) suggests negligible spectral overlap. In contrast, both FIR(P2/P1) and FIR(P5/P4) (Figs. 11(a) and (c)) exhibit moderate y_0 values (~0.56 and ~0.22, respectively), indicating a partial overlap between nearby emission bands.

The significant energy gaps observed in the analyzed FIR curves suggest that temperature-dependent intensity ratios can yield high sensitivity. Although excitation in the NIR confirms the strong thermometric potential of this material [43,63–65], the primary advantage of Nd^{3+}-doped systems lies in their ability to operate within the BWs. Typically, thermally coupled Stark sublevel luminescent transitions are employed for this purpose. In addition to the commonly

used Stark sublevel transitions, this study also explored the P1 and P3 emission lines, corresponding to the $^4F_{3/2} \rightarrow {}^4I_{9/2}$ and $^4F_{5/2} \rightarrow {}^4I_{11/2}$ transitions, respectively.

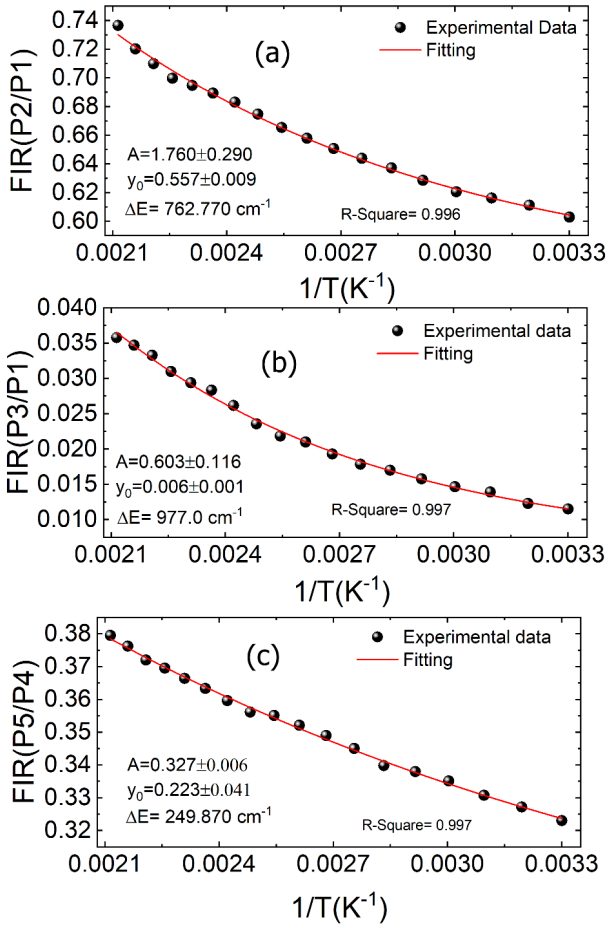


Figure 11. Plot of FIRs (a) P2/P1, (b) P3/P1, and (c) P5/P4 as a function of 1/T.

The performance of each FIR-based sensing scheme was evaluated by calculating its corresponding S_a and S_r curves. For schemes based on thermally coupled energy levels, the sensitivity curves were derived using the parameters ΔE, y_0, and A, as defined in Equations (S.6) and (S.7). In contrast, for the methodology based on Stark sublevels, the sensitivity curves were determined using empirical parameters (a and b) applied to Equations (S.9) and (S.10). Fig. 12 shows that all FIR schemes investigated in this study exhibited peak S_a and S_r values within the physiological range, except for the S_a of FIR(P3/P1), which demonstrated its maximum sensitivity outside this interval. The S_r values for FIR(P2/P1), FIR(P3/P1), and FIR(P5/P4) were 1.19 $\%K^{-1}$, 1.53 $\%K^{-1}$, and 0.39 $\%K^{-1}$, respectively. Table 3 provides a comparative analysis of the detection performance of the FIR schemes reported in this study with other Nd^{3+}-doped materials previously documented under NIR excitation. These results demonstrate that the S_r achieved in this study outperform those reported in earlier Nd^{3+}-based systems. Notably, the FIR(P3/P1) scheme yielded the highest S_r ever reported for a Nd^{3+}-doped material under NIR excitation.

It is important to note that the S_r is considered the most reliable metric for evaluating the performance of luminescent temperature sensors, as it enables direct comparison across different FIR schemes. Among the tested schemes, the FIR(P3/P1) ratio arising from thermal coupling between the $^4F_{3/2}$ and $^4F_{5/2}$ levels exhibited the highest sensitivity and overall best

performance. In contrast, FIR schemes based on Stark sublevels exhibited lower S_r values, both within the physiological range and across the full temperature interval studied.

The performance differences among the three FIRs can be attributed to the energy gaps between the levels involved. FIR(P3/P1), which includes transitions from both the $^4F_{5/2}$ and $^4F_{3/2}$ states, has the largest ΔE (977 cm^{-1}), followed by FIR(P2/P1) (~763 cm^{-1}) and FIR(P5/P4) (~250 cm^{-1}), both of which involve Stark sublevels of the $^4F_{3/2}$ state. Despite its high ΔE, FIR(P3/P1) exhibits a higher relative sensitivity S_r, owing to the opposing thermal behavior of the P3 and P1 emissions, where P3 increases while P1 decreases with temperature. Combined with minimal spectral overlap, this results in a more pronounced variation in FIR with temperature, and thus improved thermometric performance [66,67].

To further assess the thermometric performance and examine the effect of spectral broadening on sensitivity evaluation, the FIR(P3/P1) analysis was extended using integrated PL intensities over the full emission bands of the $^4F_{5/2} \rightarrow {}^4I_{11/2}$ and $^4F_{3/2} \rightarrow {}^4I_{9/2}$ transitions. This approach captures the contribution from all Stark sublevels within each multiplet transition, thereby offering a more comprehensive representation of the luminescence response. The resulting absolute and relative sensitivities at 303 K were calculated as 1.17×10^{-4} K^{-1} and 0.90 % K^{-1}, respectively. At the maximum measured temperature of 473 K, the values are 1.37×10^{-4} K^{-1} and 0.37 % K^{-1}. These values were compared with those derived using absolute peak intensities, where the maximum S_r reached 1.53 % K^{-1} at 303 K. The observed reduction in sensitivity when using integrated intensities is attributed to the inclusion of broader emission features arising from the full set of thermally populated Stark sublevels. In contrast, absolute peak intensity-based FIR values rely on a single emission line within each manifold, which may disproportionately reflect intensity changes associated with only one Stark transition. Integrated intensities naturally smooth out sharp spectral variations and provide a more temperature-averaged response, particularly relevant for thermally coupled levels with overlapping sublevel transitions. This analysis demonstrates that integrated intensities offer valuable insights into thermal population dynamics and confirm the robustness and consistency of the Nd^{3+}-based FIR sensing mechanism.

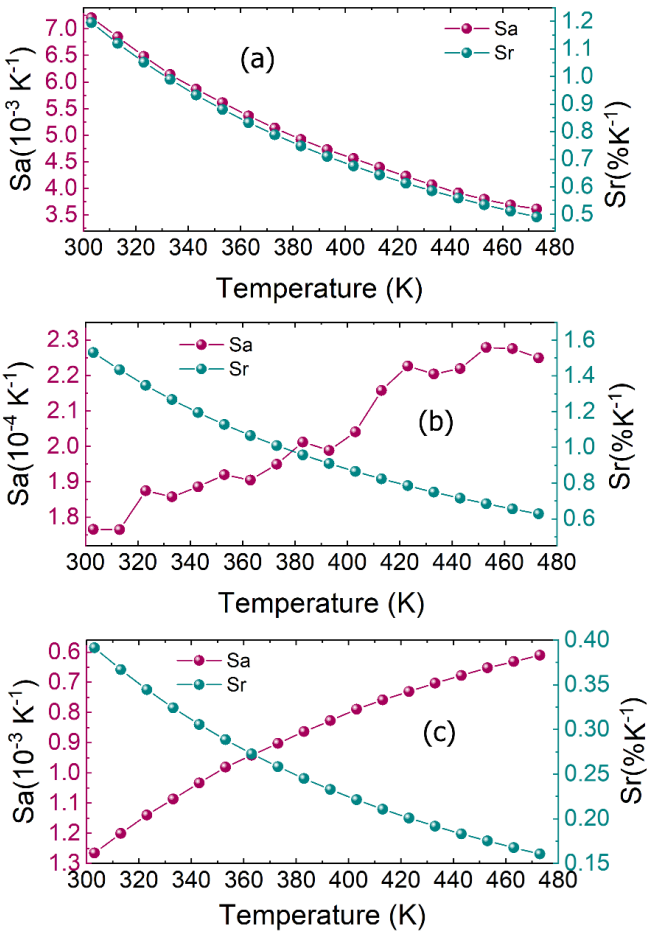


Figure 12. Variation of S_a and S_r as a function of the 303-473 K temperature range: (a) from FIR(P2/P1), (b) from FIR(P3/P1), and (c) from FIR(P5/P4).

Table 3. Comparative study of the detection capabilities of Nd^{3+}-doped hosts under NIR excitation.

Host matrix	λ_{exc} (nm)	FIR (emitting levels)	Temperature Range (K)	S_r (% K^{-1})	Ref.
LBGW	808	$^4F_{5/2}$ /$^4F_{3/2}$ $^4F_{3/2}$(P2) /$^4F_{3/2}$(P1) $^4F_{3/2}$(P5) /$^4F_{3/2}$(P4)	303-473	1.53 1.19 0.39	This work
$Ca_8NaBi(PO_4)_6F_2$	808	$^4F_{3/2}$(2)/$^4F_{3/2}$(1) $^4F_{3/2}$/$^4F_{5/2}$	303–403	0.10 0.96	[50]
$LiBaPO_4$	800	$^4F_{3/2}$ (2)/ $^4F_{3/2}$ (1)	294–423	0.097	[62]
Y_2O_3	800	$^4F_{3/2}$ (2)/ $^4F_{3/2}$ (1)	293–333	0.34	[26]
YVO_4	808	$^4F_{3/2}$ (2)/ $^4F_{3/2}$ (1)	298–333	0.25	[25]
$YNbO_4$	808	$^4F_{3/2}$ (2)/$^4F_{3/2}$(1)	303–473	0.29	[10]
YAG/Fe_3O_4	813	$^4F_{3/2}$ (2)/ $^4F_{3/2}$ (1)	297–330	0.15	[68]
$LiNdP_4O_{12}$	800	$^4F_{3/2}$ (2)/ $^4F_{3/2}$ (1)	250–500	0.25	[24]
LaF_3	808	$^4F_{3/2}$ (2)/ $^4F_{3/2}$ (1)	283–333	0.1	[13]
$Y_3Al_5O_{12}$	808	$^4F_{3/2}$ (2)/ $^4F_{3/2}$ (1)	288–343	0.17	[23]
$KGd(WO_4)_2$	808	$^4F_{3/2}$(2) / $^4F_{3/2}$(1)	298–333	0.16	[69]

To assess the performance of a thermometer, key parameters such as measurement uncertainty, reproducibility, and sensitivity to experimental conditions must be considered [70]. Of these factors, temperature uncertainty (δT) is particularly important, as it defines the minimum variation in temperature that can be detected in practical conditions. The δT is calculated using the following expression [71]:

$$\delta T = \frac{1}{S_r} \cdot \frac{\delta FIR}{FIR} = \frac{1}{S_r} \cdot \frac{\sqrt{2}}{SNR} \quad . \tag{8}$$

The term $\frac{\delta FIR}{FIR}$ represents the relative uncertainty in the intensity ratio, and SNR is the signal-to-noise ratio of the detection system. Figs. 13(a) and 13(b) illustrate the variation of the δT as a function of temperature (303–473 K) for LBGW:3 at.% Nd^{3+} phosphors, corresponding to FIR(P2/P1), FIR(P3/P1), and FIR(P5/P4), respectively. Specifically, the minimum resolution obtained for FIR(P3/P1) at 303 K is 8.86×10^{-5} K (see Fig. 13(a)), demonstrating the high precision of the method. These findings confirm that LBGW:3 at.% Nd^{3+} phosphors are highly promising for temperature sensing applications. Furthermore, this result highlights that employing Stark sublevels in FIR analysis is an effective strategy for improving thermometric resolution.

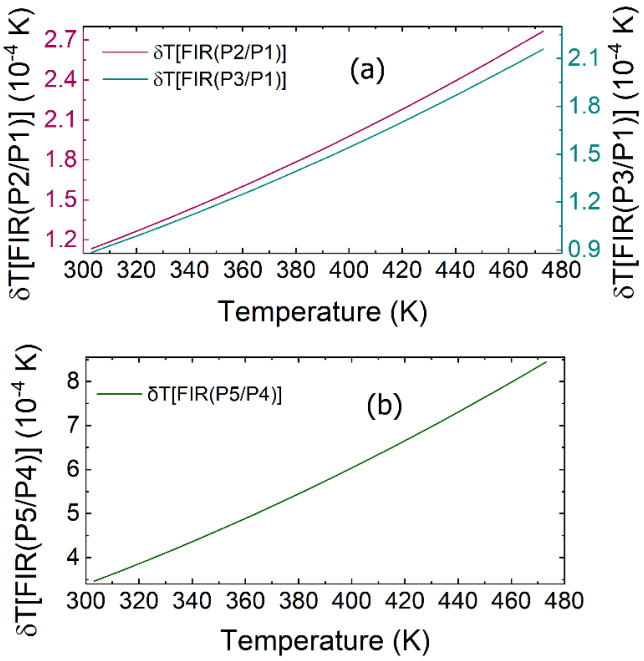


Figure 13. Variation of δT for (a) FIR(P2/P1) and FIR(P3/P1), (b) FIR(P5/P4) as a function of temperature (303-473 K) for LBGW:3 at.% Nd^{3+} phosphors.

To evaluate the repeatability of optical thermometry for LBGW:3 at.% Nd^{3+} phosphor, FIR values were measured while varying the temperature from 303 K (cooling) to 473 K (heating) over six cycles. The experimental results for FIR(P2/P1), FIR(P3/P1), and FIR(P5/P4) are presented in Figs. 14(a), 14(b), and 14(c), respectively. The repeatability (R) is calculated using the following formula [72]:

$$R = \left(1 - \frac{Max\,(\Delta_k - \Delta_l)}{\Delta_k}\right) \times 100\% \ , \tag{9}$$

where Δ_k and Δ_l represent the mean and experimental FIR values at a given temperature, respectively. The calculated deviations were minimal: FIR(P2/P1) varied by 6.55% (cooling) and 4.50% (heating), FIR(P3/P1) by 5.61% and 6.08%, and FIR(P5/P4) by 6.38% and 5.17%, respectively. These low fluctuation levels confirm the high optical stability and excellent reversibility of the phosphor under cyclic thermal stress. Such repeatability is particularly relevant for biomedical applications that require accurate, stable, and real-time temperature monitoring. Therefore, the LBGW:Nd^{3+} phosphors present strong potential for integration into optical temperature sensing systems and may serve as a promising candidate for future development toward advanced biological applications.

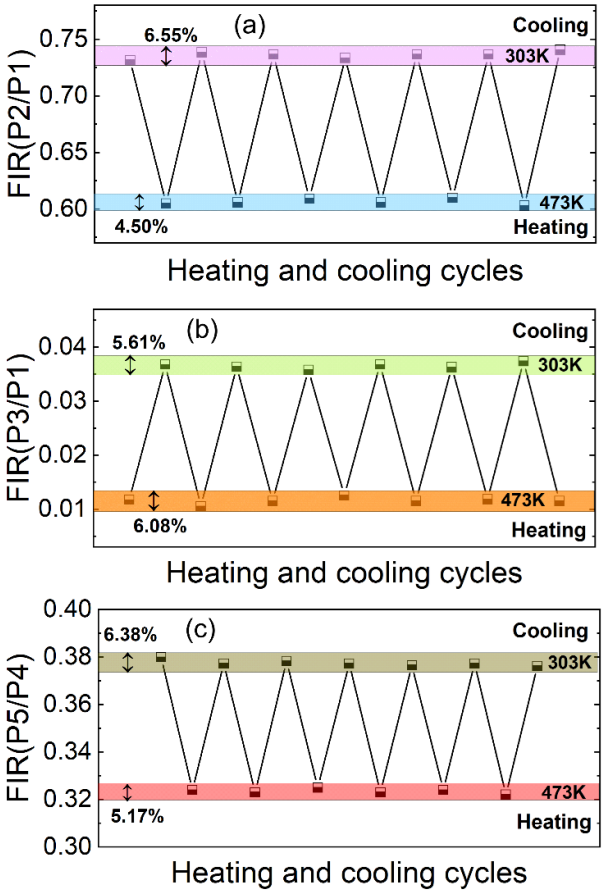


Figure 14. Repeatability of FIR ratios for LBGW:3 at.% Nd^{3+} phosphors during heating (473 K) and cooling (303 K) Cycles: (a) FIR(P2/P1), (b) FIR(P3/P1), and (c) FIR(P5/P4).

Conclusion

LBGW:Nd^{3+} phosphors were successfully synthesized using the conventional solid-state reaction method and thoroughly characterized, focusing on their photoluminescence properties under 808 nm excitation for optical temperature sensing applications. The NIR emission spectra exhibited distinct bands corresponding to radiative transitions from the $^4F_{3/2}$ and $^4F_{5/2}$ excited states to the $^4I_{9/2}$ and $^4I_{11/2}$ levels of Nd^{3+} ions. The optical thermometric performance of these phosphors was evaluated over the 303–473 K temperature range using the FIR method, based on thermal coupling between specific excited states. Among the various FIR-based sensing schemes examined, the FIR(P3/P1) scheme, involving transitions from the $^4F_{5/2}$ and $^4F_{3/2}$ levels, demonstrated the highest S_r of 1.53 $\%K^{-1}$ within the physiological temperature range. This value exceeds previously reported sensitivities for Nd^{3+}-doped materials, highlighting a significant enhancement in performance. These results not only validate the performance of LBGW:Nd^{3+} phosphors for high-sensitivity, all-infrared optical thermometry, particularly within the I-BW and II-BW where NIR light penetrates biological tissues most efficiently but also pave the way for their integration into biocompatible and minimally invasive sensing platforms.

Acknowledgments

This publication is supported by the predoctoral program AGAUR-FI ajuts (2024 FI-1 00193) Joan Oró, which is backed by the Secretariat of Universities and Research of the Department of Research and Universities of the Generalitat of Catalonia, as well as the

European Social Plus Fund. This work was also funded by Grant PID2022-141499OB-100 , supported by MICIU/AEI/10.13039/501100011033 and co-funded by FEDER/UE. The financial support provided by the Helmholtz Association is gratefully acknowledged: (i) a Recruitment Initiative Fellowship for B.S.R.; (ii) the funding of chemical synthesis equipment from the Helmholtz Materials Energy Foundry (HEMF); and (iii) Research Field Energy – Program Materials and Technologies for the Energy Transition – Topic 1 Photovoltaics (38.01.02). KIT is also grateful to financial support from the Helmholtz Association – Materials and Technologies for the Energy Transition (MTET) – Topic 1 Photovoltaics (38.01.05).

References

[1] X.D. Wang, O.S. Wolfbeis, R.J. Meier, Luminescent probes and sensors for temperature, Chem. Soc. Rev. 42 (2013) 7834–7869.

[2] X. Tian, X. Wei, Y. Chen, C. Duan, M. Yin, Temperature sensor based on ladder-level assisted thermal coupling and thermal-enhanced luminescence in $NaYF_4$: Nd^{3+}, Opt. Express. 22 (2014) 30333.

[3] C.D.S. Brites, A. Millán, L.D. Carlos, Lanthanides in luminescent thermometry, in: Handb. Phys. Chem. Rare Earths, Elsevier. (2016) 339–427.

[4] M.D. Dramićanin, Sensing temperature via downshifting emissions of lanthanide-doped metal oxides and salts. A review, Methods Appl. Fluoresc. 4 (2016) 042001.

[5] H. Kusama, O.J. Sovers, T. Yoshioka, Line shift method for phosphor temperature measurements, Jpn. J. Appl. Phys. 15 (1976) 2349.

[6] J.S. McCormack, Remote optical measurement of temperature using luminescent materials, Electron. Lett. 17 (1981) 630–631.

[7] I.E. Kolesnikov, A.A. Kalinichev, M.A. Kurochkin, D. V Mamonova, E.Y. Kolesnikov, E. Lähderanta, M.D. Mikhailov, Bifunctional heater-thermometer Nd^{3+}-doped nanoparticles with multiple temperature sensing parameters, Nanotechnology. 30 (2019) 145501.

[8] V. Lojpur, Ž. Antić, M.D. Dramićanin, Temperature sensing from the emission rise times of Eu^{3+} in SrY_2O_4, Phys. Chem. Chem. Phys. 16 (2014) 25636–25641.

[9] S. Allison, S. Goedeke, M. Cates, T. Bonsett, D. Smith, A. Brewington, T. Bencic, Phosphor thermometry in an operating turbine engine, in: 41st AIAA/ASME/SAE/ASEE Jt. Propuls. Conf. Exhib. (2005) 4374.

[10] L.Đ. Far, S.R. Lukić-Petrović, V. Đorđević, K. Vuković, E. Glais, B. Viana, M.D. Dramićanin, Luminescence temperature sensing in visible and NIR spectral range using Dy^{3+} and Nd^{3+} doped $YNbO_4$, Sensors Actuators A Phys. 270 (2018) 89–96.

[11] S.A. Wade, J.C. Muscat, S.F. Collins, G.W. Baxter, Nd^{3+}-doped optical fiber temperature sensor using the fluorescence intensity ratio technique, Rev. Sci. Instrum. 70 (1999) 4279–4282.

[12] S.A. Wade, S.F. Collins, G.W. Baxter, Fluorescence intensity ratio technique for optical fiber point temperature sensing, J. Appl. Phys. 94 (2003) 4743–4756.

[13] U. Rocha, C. Jacinto da Silva, W. Ferreira Silva, I. Guedes, A. Benayas, L. Martinez Maestro, M. Acosta Elias, E. Bovero, F.C.J.M. van Veggel, J.A. Garcia Sole, Subtissue thermal sensing based on neodymium-doped LaF_3 nanoparticles, ACS Nano. 7 (2013) 1188–1199.

[14] L. Marciniak, W. Strek, Y. Guyot, D. Hreniak, Synthesis and luminescent properties of $La_{1-x}Nd_xP_5O_{14}$ nanocrystals, Phys. Chem. Chem. Phys. 16 (2014) 18004–18009.

[15] S. Balabhadra, M.L. Debasu, C.D.S. Brites, L.A.O. Nunes, O.L. Malta, J. Rocha, M. Bettinelli, L.D. Carlos, Boosting the sensitivity of Nd^{3+}-based luminescent nanothermometers, Nanoscale. 7 (2015) 17261–17267.

[16] A.C. Brandão-Silva, M.A. Gomes, Z.S. Macedo, J.F.M. Avila, J.J. Rodrigues Jr, M.A.R.C. Alencar, Multiwavelength fluorescence intensity ratio nanothermometry: High sensitivity over a broad temperature range, J. Phys. Chem. C. 122 (2018) 20459–20468.

[17] E. Hemmer, P. Acosta-Mora, J. Mendez-Ramos, S. Fischer, Optical nanoprobes for biomedical applications: shining a light on upconverting and near-infrared emitting nanoparticles for

667 imaging, thermal sensing, and photodynamic therapy, J. Mater. Chem. B. 5 (2017) 4365–4392.
668 [18] B. del Rosal, E. Ximendes, U. Rocha, D. Jaque, In vivo luminescence nanothermometry: from
669 materials to applications, Adv. Opt. Mater. 5 (2017) 1600508.
670 [19] D. Jaque, L.M. Maestro, B. del Rosal, P. Haro-Gonzalez, A. Benayas, J.L. Plaza, E.M.
671 Rodríguez, J.G. Solé, Nanoparticles for photothermal therapies, Nanoscale. 6 (2014) 9494–
672 9530.
673 [20] J. Rocha, C.D.S. Brites, L.D. Carlos, Lanthanide organic framework luminescent
674 thermometers, Chem. Eur. J. 22 (2016) 14782–14795.
675 [21] C. Wang, Y. Jin, L. Yuan, H. Wu, G. Ju, Z. Li, D. Liu, Y. Lv, L. Chen, Y. Hu, A
676 spatial/temporal dual-mode optical thermometry platform based on synergetic luminescence of
677 Ti^{4+}-Eu^{3+} embedded flexible 3D micro-rod arrays: High-sensitive temperature sensing and
678 multi-dimensional high-level secure anti-counterfeiting, Chem. Eng. J. 374 (2019) 992–1004.
679 [22] X. Zhang, Y. Huang, M. Gong, Dual-emitting Ce^{3+}, Tb^{3+} co-doped LaOBr phosphor:
680 luminescence, energy transfer and ratiometric temperature sensing, Chem. Eng. J. 307 (2017)
681 291–299.
682 [23] A. Benayas, B. Del Rosal, A. Pérez-Delgado, K. Santacruz-Gómez, D. Jaque, G.A. Hirata, F.
683 Vetrone, Nd: YAG near-infrared luminescent nanothermometers, Adv. Opt. Mater. 3 (2015)
684 687–694.
685 [24] L. Marciniak, K. Prorok, A. Bednarkiewicz, A. Kowalczyk, D. Hreniak, W. Strek, Water
686 dispersible $LiNdP_4O_{12}$ nanocrystals: New multifunctional NIR–NIR luminescent materials for
687 bio-applications, J. Lumin. 176 (2016) 144–148.
688 [25] I.E. Kolesnikov, E. V Golyeva, A.A. Kalinichev, M.A. Kurochkin, E. Lähderanta, M.D.
689 Mikhailov, Nd^{3+} single doped YVO_4 nanoparticles for sub-tissue heating and thermal sensing
690 in the second biological window, Sensors Actuators B Chem. 243 (2017) 338–345.
691 [26] M.A. Gomes, I.S. Carvalho, L.F.A. Domingos, A.C. Brandão-Silva, J.F.M. Avila, J.J.
692 Rodrigues Jr, M.A.R.C. Alencar, M.E.G. Valerio, Z.S. Macedo, Temperature-sensitive
693 luminescence of Y_2O_3: Nd^{3+} nanocrystals produced by an eco-friendly route, Opt. Mater.
694 (Amst). 89 (2019) 536–542.
695 [27] G. Gao, D. Busko, S. Kauffmann-Weiss, A. Turshatov, I.A. Howard, B.S. Richards, Wide-
696 range non-contact fluorescence intensity ratio thermometer based on Yb^{3+}/Nd^{3+} co-doped
697 La_2O_3 microcrystals operating from 290 to 1230 K, J. Mater. Chem. C. 6 (2018) 4163–4170.
698 [28] G. Gao, D. Busko, N. Katumo, R. Joseph, E. Madirov, A. Turshatov, I.A. Howard, B.S.
699 Richards, Ratiometric Luminescent Thermometry with Excellent Sensitivity over a Broad
700 Temperature Range Utilizing Thermally-Assisted and Multiphoton Upconversion in Triply-
701 Doped La_2O_3:Yb^{3+}/Er^{3+}/Nd^{3+}, Adv. Opt. Mater. 9 (2021).
702 [29] A.A. Kalinichev, M.A. Kurochkin, E. V Golyeva, A. V Kurochkin, E. Lähderanta, M.D.
703 Mikhailov, I.E. Kolesnikov, Near-infrared emitting YVO_4: Nd^{3+} nanoparticles for high
704 sensitive fluorescence thermometry, J. Lumin. 195 (2018) 61–66.
705 [30] B. Cao, Y. Bao, Y. Liu, J. Shang, Z. Zhang, Y. He, Z. Feng, B. Dong, Wide-range and highly-
706 sensitive optical thermometers based on the temperature-dependent energy transfer from Er to
707 Nd in Er/Yb/Nd codoped $NaYF_4$ upconversion nanocrystals, Chem. Eng. J. 385 (2020) 123906.
708 [31] W. Xu, Y. Hu, L. Zheng, Z. Zhang, W. Cao, H. Liu, X. Wu, Enhanced NIR-NIR luminescence
709 from $CaWO_4$: Nd^{3+}/Yb^{3+} phosphors by Li^+ codoping for thermometry and optical heating, J.
710 Lumin. 208 (2019) 415–423.
711 [32] W. Xu, H. Qi, L. Zheng, Z. Zhang, W. Cao, Multifunctional nanoparticles based on the
712 Nd^{3+}/Yb^{3+} codoped $NaYF_4$, Opt. Lett. 40 (2015) 5678–5681.
713 [33] Z. Zhang, Y. Shen, S. Slimi, X. Mateos, S. Wang, Photoluminescence properties and
714 temperature sensing of Pr^{3+}-Doped $Li_3Ba_2Gd_3(WO_4)_8$ quaternary tungstate, Ceram. Int. (2024)
715 9092-9099.
716 [34] W.L. Guo, Y.T. Jiao, P.S. Wang, Q. Liu, S. Liu, F. Hou, Energy transfer and spectroscopic
717 characterization of new green emitting $Li_3Ba_2Gd_3(WO_4)_8$: Tb^{3+} phosphor, in: Solid State
718 Phenom., Trans Tech Publ. (2018) 686–691.
719 [35] X.-H. Pei, Y.-Y. Zhao, K. Liu, Exploring a new Sm^{3+}-activated tungstate phosphor with
720 thermally stable photoluminescence, J. Iran. Chem. Soc. 20 (2023) 2269–2275.
721 [36] A. Douzi, S. Slimi, E. Madirov, A. Turshatov, B.S. Richards, R.M. Solé, M. Aguiló, F. Díaz, E.

Ben Salem, X. Mateos, Structure and luminescence properties of Dy^{3+} doped quaternary tungstate $Li_3Ba_2Gd_3(WO_4)_8$ for application in wLEDs, RSC Adv. 13 (2023) 23772–23787.
[37] Z. Zhang, A. Douzi, S. Slimi, E. Madirov, A. Arouri, V. Llamas, J.M. Serres, R.M. Solé, M. Aguiló, F. Díaz, Optical Properties and Judd-Ofelt Analysis of a Novel Red-Emitting Monoclinic $Li_3Ba_2Gd_3(WO_4)_8$: Eu^{3+} Phosphor, Inorg. Chem. Commun. (2024) 112230.
[38] R.D. Shannon, Revised effective ionic radii and systematic studies of interatomic distances in halides and chalcogenides, Acta Crystallogr. Sect. A Cryst. Physics, Diffraction, Theor. Gen. Crystallogr. 32 (1976) 751–767.
[39] R.D. Shannon, F.L.D. Shannon, Dielectric polarizabilities of ions in oxides and fluorides Dielectric polarizabilities of ions in oxides and fluorides, 348 (1993) 348-366.
[40] H. Li, G.J. Wang, L.Z. Zhang, Y.S. Huang, G.F. Wang, Growth and spectral properties of Nd^{3+}:$Li_3Ba_2Y_3(WO_4)_8$ crystal, Mater. Res. Innov. 14 (2010) 419–422.
[41] P. Huang, X. Wang, X. Liang, J. Yang, C. Zhang, D. Kong, W. Wang, Nano-, micro-, and macroscale drug delivery systems for cancer immunotherapy, Acta Biomater. 85 (2019) 1–26.
[42] E.I. Wafa, J.H. Wilson-Welder, R.L. Hornsby, J.E. Nally, S.M. Geary, N.B. Bowden, A.K. Salem, Poly (diaminosulfide) microparticle-based vaccine for delivery of leptospiral antigens, Biomacromolecules. 21 (2020) 534–544.
[43] A. Douzi, S. Slimi, P. Loiko, V. Llamas, J.M. Serres, R.M. Solé, M. Aguiló, F. Díaz, E. Ben Salem, X. Mateos, Temperature sensing by means of a near-infrared luminescent $Ca_8NaBi(PO_4)_6F_2$: Nd^{3+} fluorapatite phosphor, J. Mater. Sci. Mater. Electron. 35 (2024) 890.
[44] J. Hanuza, L. Macalik, Polarized infra-red and Raman spectra of monoclinic α-$KLn(WO_4)_2$ single crystals (Ln = Sm—Lu, Y), Spectrochim. Acta Part A Mol. Spectrosc. 43 (1987) 361–373.
[45] Y. V Baklanova, O.A. Lipina, L.G. Maksimova, A.P. Tyutyunnik, I.I. Leonidov, T.A. Denisova, V.G. Zubkov, Nd^{3+}, Ho^{3+}-codoped garnet-related $Li_7La_3Hf_2O_{12}$ phosphor with NIR luminescence, Spectrochim. Acta Part A Mol. Biomol. Spectrosc. 180 (2017) 105–109.
[46] A. Balakrishna, H.C. Swart, R.E. Kroon, O.M. Ntwaeaborwa, Host sensitized near-infrared emission in Nd^{3+} doped different alkaline-sodium-phosphate phosphors, Phys. B Condens. Matter. 535 (2018) 29–34.
[47] G. Anoop, K.M. Krishna, M.K. Jayaraj, The effect of Mg incorporation on structural and optical properties of Zn_2GeO_4: Mn phosphor, J. Electrochem. Soc. 155 (2007) J7.
[48] S. Landi Jr, I.R. Segundo, E. Freitas, M. Vasilevskiy, J. Carneiro, C.J. Tavares, Use and misuse of the Kubelka-Munk function to obtain the band gap energy from diffuse reflectance measurements, Solid State Commun. 341 (2022) 114573.
[49] J. Tauc, A. Menth, States in the gap, J. Non. Cryst. Solids. 8 (1972) 569–585.
[50] A. Douzi, S. Slimi, P. Loiko, V. Llamas, J.M. Serres, R.M. Solé, M. Aguiló, F. Díaz, E. Ben Salem, X. Mateos, Temperature sensing by means of a near-infrared luminescent $Ca_8NaBi(PO_4)_6F_2$:Nd^{3+} fluorapatite phosphor, J. Mater. Sci. Mater. Electron. 35 (2024) 1–16.
[51] M. Shoaib, G. Rooh, N. Chanthima, H.J. Kim, J. Kaewkhao, Luminescence properties of Nd^{3+} ions doped P_2O_5-Li_2O_3-GdF_3 glasses for laser applications, Optik (Stuttg). 199 (2019) 163218.
[52] A.M. Smith, M.C. Mancini, S. Nie, Second window for in vivo imaging, Nat. Nanotechnol. 4 (2009) 710–711.
[53] G. Jiang, X. Wei, S. Zhou, Y. Chen, C. Duan, M. Yin, Neodymium doped lanthanum oxysulfide as optical temperature sensors, J. Lumin. 152 (2014) 156–159.
[54] G. Chen, T.Y. Ohulchanskyy, S. Liu, W.-C. Law, F. Wu, M.T. Swihart, H. Ågren, P.N. Prasad, Core/shell $NaGdF_4$: Nd^{3+}/$NaGdF_4$ nanocrystals with efficient near-infrared to near-infrared downconversion photoluminescence for bioimaging applications, ACS Nano. 6 (2012) 2969–2977.
[55] G. Blasse, Energy transfer between inequivalent Eu^{2+} ions, J. Solid State Chem. 62 (1986) 207–211.
[56] D.L. Dexter, J.H. Schulman, Theory of concentration quenching in inorganic phosphors, J. Chem. Phys. 22 (1954) 1063–1070.
[57] F. Auzel, Multiphonon-assisted anti-Stokes and Stokes fluorescence of triply ionized rare-earth ions, Phys. Rev. B. 13 (1976) 2809.
[58] R.S. Melo, J.C. S Filho, N.S. Camilo, T.I. Rubio, D. Manzani, A.A. Andrade, Nd^{3+}-doped

fluoroborontellurite glass as a near-infrared optical thermometer, Mater. Res. Bull. 157 (2023) 112031.
[59] N. Rakov, G.S. Maciel, Near-infrared emission and optical temperature sensing performance of Nd^{3+}: SrF_2 crystal powder prepared by combustion synthesis, J. Appl. Phys. 121 (2017).
[60] R.S. Silva, D.L. Ferreira, E.M. Alves, T.A. Maia, A.S. Silva, E. V Guimarães, G.A. Azevedo, N.S. Camilo, A.A. Andrade, Synthesis and optical properties of $CsPbI_3$ perovskite nanocrystals in borosilicate glass doped with Nd^{3+} ions, J. Non. Cryst. Solids. 606 (2023) 122188.
[61] W. Xu, H. Qi, L. Zheng, Z. Zhang, W. Cao, Multifunctional nanoparticles based on the Nd^{3+}/Yb^{3+} codoped $NaYF_4$, Opt. Lett. 40 (2015) 5678–5681.
[62] A.S. Laia, D.A. Hora, M. V. Marcos, Y. Xing, J.J. Rodrigues, G.S. Maciel, M.A.R.C. Alencar, Nd^{3+}-doped $LiBaPO_4$ phosphors for optical temperature sensing within the first biological window: A new strategy to increase the sensitivity, Chem. Eng. J. 399 (2020) 125742.
[63] Y. Zhang, Q. Wang, C. Sun, H. Tian, H. Zhu, X. Yang, H. Wang, H. Liu, Near-infrared luminescence and temperature sensing properties of $Sc_2Mo_3O_{12}$: $Nd^{3+}/Yb^{3+}/Ho^{3+}$ phosphor, Spectrochim. Acta Part A Mol. Biomol. Spectrosc. (2025) 125869.
[64] M. Suta, Ž. Antić, V. Đorđević, S. Kuzman, M.D. Dramićanin, A. Meijerink, Making Nd^{3+} a sensitive luminescent thermometer for physiological temperatures—an account of pitfalls in Boltzmann thermometry, Nanomaterials. 10 (2020) 543.
[65] W. Xu, Q. Song, L. Zheng, Z. Zhang, W. Cao, Optical temperature sensing based on the near-infrared emissions from Nd^{3+}/Yb^{3+} codoped $CaWO_4$, Opt. Lett. 39 (2014) 4635–4638.
[66] M. Pudovkin, E. Oleynikova, A. Kiiamov, M. Cherosov, M. Gafurov, Nd^{3+}, Yb^{3+}: YF_3 optical temperature nanosensors operating in the biological windows, Materials (Basel). 16 (2022) 39.
[67] M. Bravo, S. Yang, D. Wen, S. Krzyzowska, F. Taemaitree, S. Zaman, B. Fortuni, S. Rocha, P. Mulvaney, H. Uji-i, Neodymium-Doped Nanocrystals for Diffraction-limited in vitro Temperature Sensing, BioRxiv. (2024) 2002–2024.
[68] E.M. Tejeda, M. Arámburo, E. Vargas, O.E. Contreras, G.A. Hirata, Novel bifunctional Nd: YAG/Fe_3O_4 nanocomposite as nanothermometer/nanoheater for potential biomedical applications, J. Phys. D. Appl. Phys. 51 (2018) 40LT01.
[69] O. Savchuk, J.J. Carvajal, L.G. De la Cruz, P. Haro-González, M. Aguiló, F. Díaz, Luminescence thermometry and imaging in the second biological window at high penetration depth with Nd: $KGd(WO_4)_2$ nanoparticles, J. Mater. Chem. C. 4 (2016) 7397–7405.
[70] M.D. Dramićanin, Trends in luminescence thermometry, J. Appl. Phys. 128 (2020).
[71] Z. Wang, D. Ananias, A. Carné-Sánchez, C.D.S. Brites, I. Imaz, D. Maspoch, J. Rocha, L.D. Carlos, Lanthanide–Organic Framework Nanothermometers Prepared by Spray-Drying, Adv. Funct. Mater. 25 (2015) 2824–2830.
[72] J. Chen, W. Zhang, S. Cui, X. Peng, F. Hu, R. Wei, H. Guo, D. Huang, Up-conversion luminescence properties and temperature sensing performances of $Ba_5Y_8Zn_4O_{21}$: Yb^{3+}, Er^{3+} phosphors, J. Alloys Compd. 875 (2021) 159922.